APPLICATIONS OF POTENTIAL THEORY COMPUTATIONS TO TRANSONIC AEROELASTICITY

John W. Edwards
NASA Langley Research Center
Hampton, Virginia 23665-5225

ICAS-86-2.9.1

Abstract

Unsteady aerodynamic and aeroelastic stability calculations based upon transonic small disturbance (TSD) potential theory are presented. Results from the two-dimensional XTRAN2L code and the three-dimensional XTRAN3S code are compared with experiment to demonstrate the ability of TSD codes to treat transonic effects. The necessity of nonisentropic corrections to transonic potential theory is demonstrated. Dynamic computational effects resulting from the choice of grid and boundary conditions are illustrated. Unsteady airloads for a number of parameter variations including airfoil shape and thickness, Mach number, frequency, and amplitude are given. Finally, samples of transonic aeroelastic calculations are given. A key observation is the extent to which unsteady transonic airloads calculated by inviscid potential theory may be treated in a locally linear manner.

List of Symbols

AR	aspect ratio
C_p	pressure coefficient
C_p^*	critical pressure coefficient
ΔC_p	unsteady lifting pressure coefficient
c	airfoil chord, m
c_ℓ	lift coefficient
c_{ℓ_α}	first harmonic lift coefficient due to pitch, per radian
c_r	wing reference chord, m
h	nondimensional airfoil plunge displacement
k	reduced frequency, $\omega c/2V$
M	free stream Mach number
Re	Reynolds number based on chord, Uc/υ
r	airfoil function, $z = r(x,t)$ on the airfoil surface, m
s	$\sigma + i\omega$; Laplace transform variable, rad/sec
t	time, s
U	free stream velocity, m/s
V	speed index
x	streamwise coordinate relative to leading edge, m
y	coordinate normal to x and z, positive to right, m
z	coordinate normal to free stream, positive up, m
α	angle of attack, deg
α_m	mean angle of attack, deg
α_0	dynamic pitch angle, deg
γ	ratio of specific heats
δ	flap angle, deg
ε	airfoil thickness ratio
$\bar{\eta}$	fraction of semi-span
τ	nondimensional time in semichords traveled, $2Ut/c$
Φ	perturbation velocity potential
φ	phase angle, deg
ω	angular frequency, $2\pi f$, rad/s
υ	kinematic viscosity
$[\ldots]$	indicates jump in ...

Subscripts

LE	leading edge value
ℓ	lower surface value
TE	trailing edge value
u	upper surface value

Introduction

The field of aeroelastic response and flutter prediction has traditionally relied upon linear subsonic and supersonic unsteady aerodynamics coupled with linear descriptions of aircraft structural dynamics to perform stability analyses. In the transonic speed regime where the aerodynamic theories were not on a technically sound foundation, numerous wind tunnel tests of flutter models and flight test experience provided the confidence to operate aircraft. Due to the lack of more accurate transonic aerodynamic theory, linear unsteady airloads have been used for flutter predictions and have been reasonably successful in providing conservative flutter boundaries. Emerging aircraft designs, calling for aircraft performance objectives at maneuvering flight conditions, and seeking optimized aerodynamic and structural configurations press these traditional aeroelastic design tools beyond their accuracy limits. New aeroelastic response computational techniques based upon accurate simulation of the nonlinear transonic flow field are needed to bridge this gap.

The past decade has brought a maturing of experimental and computational capabilities aimed at filling this gap. The AGARD Structures and Materials Panel has sponsored computational efforts by defining sets of two- and three-dimensional Standard Aeroelastic Configurations[1,2]. Numerous comparisons of computed results with experimental data sets[3] are given in Reference 4. Computational methods range in complexity from modified linear theories to solutions of the Navier-Stokes equations. Due to their relative simplicity, nonlinear potential theory methods have been used most frequently. Economical finite-difference solutions of the time-accurate transonic small disturbance (TSD) potential equation were first obtained with the alternating-direction implicit (ADI) algorithm introduced in the low-frequency LTRAN2 code by Ballhaus and Goorjian[5]. The LTRAN2 algorithm has been extensively updated with a series of improvements by many researchers. The XTRAN2L code[6] solves the full frequency TSD equation and includes the capability of calculating transient aeroelastic and flutter solutions. Borland and Rizzetta[7] used the ADI algorithm in the XTRAN3S code to obtain solutions of the 3-D TSD equation for isolated wings. Surveys of applications of this

code are given by Edwards et al.[8] and by Goorjian and Guruswamy[9]. Extensions have been made to treat multiple lifting surfaces[10,11] and wing-fuselage combinations[12]. More recently, work has been reported on 3-D full potential code development by Ruo et al.[13] and by Shankar et al.[14]

The number of applications of TSD codes to unsteady aerodynamic and aeroelastic calculations makes feasible an assessment of accuracy and reliability. This paper will present a survey of results obtained with 2-D and 3-D TSD codes at the NASA Langley Research Center. The effects of shock-generated entropy and dynamic effects of computational grids will be illustrated. Typical 2-D results showing the effect of Mach number, frequency, airfoil shape, viscous boundary layer modeling and oscillation amplitude are given. Comparisons of calculated 3-D unsteady pressures with experiment are followed by examples of multiple lifting surface and wing-fuselage interference effects. Finally, examples of transonic aeroelastic and active control calculations are given which illustrate the locally linear nature of these calculated flows.

Transonic Small Disturbance Equation

Two-Dimensional Case

Most of the two-dimensional results presented were obtained using the XTRAN2L code[6] which solves the complete unsteady TSD potential equation. In terms of the scaled variables used in the code, this equation is

$$(C\Phi_T + A\Phi_X)_T = (E\Phi_X + F\Phi_X^2)_X + (\Phi_Z)_Z \qquad (1)$$

where the variables and coefficients are scaled as

$$T = \omega t \qquad \varepsilon^* = \varepsilon M^2(\gamma^* + 1)$$
$$X = x/c \qquad \gamma^* = 2 - (2 - \gamma)M^2$$
$$Z = z\varepsilon^{*1/3}/c \qquad \Phi = \phi/(cU\varepsilon^{*2/3})$$
$$C = 4k^2M^2/\varepsilon^{*2/3} \qquad E = (1-M^2)/\varepsilon^{*2/3}$$
$$A = 4kM^2/\varepsilon^{*2/3} \qquad F = -\tfrac{1}{2}M^2(\gamma^* + 1)$$

The reduced frequency k is based on semi-chord. The airfoil flow tangency and trailing wake conditions are applied on the z = 0 line and, in the small disturbance approximation, become

$$\Phi_Z^{\pm} = R_X^{\pm} + 2kR_T^{\pm} \quad ; \quad Z = 0^{\pm}, \ 0 < X < 1 \qquad (2a)$$

$$[\Phi_X] + 2k[\Phi_T] = 0 \quad ; \quad Z = 0, \ X > 1 \qquad (2b)$$

where the ± refer to the airfoil upper or lower surfaces and $R = r\varepsilon^{*1/3}/c$.

The airfoil surface slopes, R_X, required in Eq. (2a) were generated by spline curve-fitting the airfoil coordinates[1]. The curve fits were performed parametrically as a function of surface arclength, beginning at the upper surface trailing edge, around the leading edge and ending at the lower surface trailing edge. (Spline fitting the upper and lower surfaces separately can lead to erratic results near the leading edge.) No modifications to the resulting surface slopes were made to improve correlation of small perturbation calculations with experiment.

Numerical solutions of Eq. (1) were obtained using the ADI algorithm as described in Ref. 6. Monotone differencing is used to eliminate non-physical expansion shocks. Non-reflecting far-field boundary conditions[15] are implemented as follows to eliminate reflected disturbances:

upstream

$$(A/B + D/\sqrt{B})\ \Phi_T - 2\Phi_X = 0 \qquad (3a)$$

downstream

$$(-A/B + D/\sqrt{B})\ \Phi_T + 2\Phi_X = 0 \qquad (3b)$$

above (+) and below (-)

$$(BD/A)\ \Phi_X \pm \Phi_Z = 0 \qquad (3c)$$

where $B = E + 2F\Phi_X$ and $D = (4C + A^2/B)^{1/2}$.

These nonreflecting far-field boundary conditions allow the boundaries to be moved closer to the airfoil and allow greater freedom in tradeoffs among number of grid points, accuracy and expense. The default XTRAN2L grid[16] is 80 x 61 points in x,z and covers a fixed physical extent of ±20c in x and ±25c in z. An algebraic grid stretching is used to distribute grid points between the airfoil and the outer boundaries. This grid point distribution was selected to alleviate disturbances which can be generated in regions of large grid stretching. On the airfoil the x-grid has 51 grid points having a uniform spacing of 0.02c with an additional point near the leading edge.

Three-Dimensional Case

Three-dimensional calculations were performed with the XTRAN3S code[7,19] which uses a time-accurate ADI finite-difference scheme to solve the three-dimensional TSD equation

$$(C\Phi_T + A\Phi_X)_T = (E\Phi_X + F\Phi_X^2 + G\Phi_Y^2)_X + (\Phi_Y + H\Phi_X\Phi_Y)_Y + (\Phi_Z)_Z \qquad (4)$$

The nondimensional variables are

$$X = x/c_r \qquad T = \bar{k}Ut/c_r$$
$$Y = y/c_r \qquad \Phi = \phi/(Uc_r)$$
$$Z = z/c$$

Two different sets of coefficients may be defined for Eq. (4). For both cases

$$C = \bar{k}^2M^2 \qquad A = 2\bar{k}M^2 \qquad E = 1-M^2$$

where $\bar{k}$ is an arbitrary scaled frequency ($\bar{k} = 1$ herein). The coefficients for the nonlinear terms may be chosen as either

$$F = -\frac{1}{2}(\gamma + 1)M^2$$

$$G = \frac{1}{2}(\gamma - 3)M^2 \qquad (5)$$

$$H = -(\gamma - 1)M^2$$

or

$$F = -\frac{1}{2}(3 - (2 - \gamma)M^2)M^2$$

$$G = -\frac{1}{2}M^2 \qquad (6)$$

$$H = -M^2$$

The outer boundary conditions imposed on the flow-field are referred to herein as reflecting boundary conditions and are given by

upstream	$\Phi = 0$	(7a)
downstream	$\Phi_X + \bar{k}\Phi_T = 0$	(7b)
above and below	$\Phi_Z = 0$	(7c)
spanwise & wing root	$\Phi_Y = 0$	(7d)

The airfoil flow tangency condition is

$$\Phi_Z^{\pm} = R_X^{\pm} + \bar{k}\, R_T^{\pm} \;;\; Z = 0^{\pm},\; X_{LE} < X < X_{TE} \qquad (8a)$$

where $R = r/c_r$, and the wake boundary condition is

$$\lfloor \Phi_Z \rfloor = \lfloor \Phi_X + \bar{k}\Phi_T \rfloor = 0 \qquad (8b)$$

The code was run on a CDC VPS 32 computer using the computational grid described in Ref. 16 with 60 x 20 x 40 points in the x, y, and z directions. The program grid size restrictions and the reflecting boundary conditions, Eq. (7), assure that disturbances reflected by the boundaries or internal grid stretching will be present. The x, z grid was chosen to minimize the effect of the internal grid reflections[16] for $k < 0.50$. The VPS 32 is capable of scalar or vector arithmetic. The scalar version of the XTRAN3S program required 1.9 seconds of central processor unit (CPU) time per time step. Vectorizing the ADI x-sweep and a matrix manipulation routine reduced the required time to 1.2 CPU seconds per time step.

Results and Discussion

Results summarizing key features of unsteady transonic airload calculations for two- and three-dimensional flow are given. Attention is first directed at details of solution accuracy by comparison with linear theory and with the more exact Euler equations. Next, a number of geometry and amplitude effects are illustrated with results from the XTRAN2L code, followed by several results from the XTRAN3S code. Several wing planform shapes and interfering lifting surface configurations are given. Finally, the use of transonic potential equation codes for aeroelastic analysis is illustrated.

Dynamic Computational Grid Effects

Transient airloads obtained from pulsed airfoil motions allow airload frequency response functions to be calculated from a single response calculation using transfer function techniques. Of course this requires the assumption of at least local linearity of the response to the forcing function, which appears to hold widely for integrated airloads of attached flow. These features were studied in Refs. 17 and 18 which demonstrate the use of the XTRAN2L code for aeroelastic calculations. Ref. 16 uses this pulse transform technique to demonstrate key features of the relation between computational grids, boundary conditions, and dynamic calculations. The importance of controlling reflections of disturbances from the outer grid boundaries and from internal grid points is shown in figure 1. In order to compare with linear theory, the case of a flat plate airfoil at $M = 0.85$ is shown. Three lift coefficient responses resulting from quickly pitching the airfoil from 0 to 1 degree and back to 0 are given. In figures 1(a) and 1(c) the default XTRAN2L grid given above was used while in figure 1(b) an exponentially stretched grid extending ±200c in x and ±2327c in z was used. The latter grid contained 113 x 97 points in the x and z directions. Figure 1(c) was obtained using the non-reflecting boundary conditions given by Eqs. (3) while figs. 1(a) and 1(b) utilized reflecting boundary conditions similar to Eqs. (7). Of particular importance are the outer z-boundaries. The disturbance at $\tau \approx 40$ in fig. 1(a) correlates with the acoustic propagation time for travel to and return from these boundaries. The option of moving these boundaries large distances, fig. 1(b), introduces the complication of severe grid-stretching in the near-field. In this case, reflections from the outer boundaries do not occur, but disturbances seen from $\tau \approx 20$ to 50 correlate with propagation times for travel to and return from regions of the z-grid where grid spacing first becomes more than two chord-lengths. Neither of these anomalies is seen in fig. 1(c).

Figure 2 gives the c_{ℓ_α} frequency responses calculated from these transient responses. Reflections from the outer z-boundary, fig. 2(a), contaminate the unsteady airloads at low reduced frequencies, $k < 0.15$, whereas the disturbances originating from the near-field grid stretching, fig. 2(b), contaminate the airloads in the frequency range $0.2 < k < 1.0$. Figure 2(c) shows that excellent agreement with linear theory can be achieved for moderate frequencies. Other calculations verify that these features, which are most easily studied for linearized examples, carry over to nonlinear transonic calculations.

Shock-Generated Entropy

The conservative full potential and transonic small disturbance potential equations are derived with the assumptions that the flow is irrotational and isentropic. While it is recognized that entropy is generated within shock-waves, the use of potential theories to study transonic flows with weak shocks has progressed assuming that this entropy generation was a higher order effect. It is now understood that disregarding this effect can lead to serious disagreement with more exact solutions for physically interesting situations.

A common approximation in formulating the full potential equations is to impose conservation of mass and energy while satisfying the isentropic and irrotationality conditions[20]. Reference 20 shows that the shock jump conditions for such a "conservative potential" equation deviate from the Rankine-Hugoniot shock conditions as the Mach number ahead of the shock increases. In Ref. 20, the implications of this effect were studied by calculating c_ℓ versus α for a range of Mach numbers. It was known[21] that the symmetric NACA 0012 airfoil at $\alpha = 0°$ exhibited multiple solutions for $0.82 < M < 0.85$. Figure 3 shows that such ranges of multiple solutions can be found for all Mach numbers for sufficiently large angles-of-attack. More importantly for transonic aeroelasticity, it is concluded that well before α reaches values at which multiple solutions occur, the lift-curve slope, c_{ℓ_α}, has become unphysically large.

Williams et al.[22] have investigated the effect of nonunique solutions of the unsteady TSD equation. Figure 4[22] gives three different calculations of lift coefficient versus α for the NACA 0012 airfoil at $M = 0.85$. Figure 4(a) gives the upper surface pressure distributions for the three multiple solutions indicated by A, B, and C in fig. 4(b). Solution B is a symmetric nonlifting solution while the other two are lifting solutions. Figure 4(b) gives the lift coefficient versus angle-of-attack for 1.) Quasi-steady conditions, $k = 0$, and pitching oscillations for 2.) $k = 0.01$ and 3.) $k = 0.05$. Solution B is not a stable solution and diverges with an extremely large time constant to either A or C depending upon initial conditions. At $k = 0.05$ the solution oscillates about the positive lifting solution. While the average lift curve slope is not unreasonable the solution must be regarded as anomalous. In contrast, the solution for $k = 0.01$ exhibits a hysteresis loop, jumping between the two stable steady solutions. The large phase lag implied by this solution is unphysical and caution must be exercised when using such calculations.

Fuglsang and Williams[23] implemented a nonisentropic formulation for 2-D TSD theory. By modifying the expression for streamwise mass flux they were able to satisfy the Prandtl relation for Rankine-Hugoniot shocks. A modified pressure coefficient expression to account for the entropy generated across the shock and a modified wake boundary condition for entropy convection complete the nonisentropic modeling. Figure 5 shows unmodified and nonisentropic results compared to Euler and full potential results for $M = 0.84$ and $\alpha = 0.25$ deg. The nonisentropic results are very similar to the Euler results. No multiple solution conditions have been observed with the nonisentropic model and values of lift-curve slope are reasonable. Also, low frequency unsteady calculations do not exhibit the hysteresis effect shown in fig. 4(b).[23]

Gibbons et al.[24] implemented this 2-D nonisentropic model in a stripwise manner in the XTRAN3S code and demonstrated the existence of multiple solutions of the 3-D conservative protential equation. Figure 6[24] shows this feature for a series of rectangular wings having NACA 0012 airfoil sections. For $M = 0.84$, lift coefficients in response to a fast pulsed motion in angle-of-attack are plotted versus time for wing aspect ratios of 12, 24, 32, and 48. Between AR = 24 and 32, the asymptotic lift coefficient switches from zero to a nonzero value, indicating the onset of nonuniqueness. As in the 2-D case, the nonisentropic modifications eliminated the multiple solutions. The nonisentropic model also corrects unphysical lift-curve slopes for Mach numbers below those at which multiple solutions occur. Figure 7 compares c_ℓ versus α for the AR = 12 wing at $M = 0.82$. The original XTRAN3S code predicts a value of c_{ℓ_α} about twice that of the nonisentropic model, which agrees well with the FLO-57 Euler code. Chordwise pressure distributions at $\alpha = 1$ deg. are given in figure 8. For this case, the unmodified code overpredicts both the shock strength and position on the upper and lower surfaces whereas the nonisentropic modifications are in good agreement with the Euler code.

It is instructive to compare figures 3, 4, and 7 to understand the effect of shock-generated entropy upon unsteady transonic calculations. The effect of entropy varies continuously from low Mach numbers to those for which multiple solutions are found, Fig. 3. The lift-curve slope, c_{ℓ_α} can be seriously in error even outside the region of multiple solutions, fig. 7. For unsteady calculations, it would appear from fig. 4(b) that low frequency calculations are more prone to exhibiting anomalous behavior than higher frequencies. Finally, it appears that for cases where the small disturbance assumption is reasonable and vorticity is not a factor (attached flow, normal shocks) the nonisentropic modifications do a creditable job of correcting inviscid potential theory to agree with Euler equation results. Cases presented in the remainder of this paper were obtained using the unmodified codes and an effort has been made to stay away from conditions where entropy effects are significant.

Two-Dimensional Airloads

There have been numerous published results of 2-D transonic unsteady calculations. In this section, several of the more interesting results will be highlighted including effects of airfoil shape, thickness, and motion amplitude. A common thread is the degree to which transonic

unsteady airloads exhibit similarities for a broad range of such parameters.

Transonic flutter boundaries were presented in Refs. 17 and 18 for conventional and supercritical airfoils. A surprising similarity in the shape of the boundaries was observed and a detailed study of the individual airloads is given in Ref. 18. Steady pressure distributions for the conventional NACA 64A010A (10.6 percent thick) and the supercritical MBB-A3 (8.9 percent thick) for the Mach number ranges studied are shown in figure 9. The angle-of-attack was set at α = 1 deg. for the NACA 64A010A airfoil and -0.5 deg. for the MBB-A3 airfoil such that the mean lift coefficients were the same. The Mach ranges encompass flow conditions from near critical to those with moderately strong shocks. The unsteady forces for pitching and plunging motions are given in figure 10 for k = 0.15. The lift coefficients are quite similar and close to linear theory but the moment coefficients show some differences. Note that a shift of about 0.01 in Mach number brings all of the forces in very good agreement. This can be attributed to a thickness effect[18] and is consistent with a transonic similarity shift of about 0.007 in M corresponding to a ratio in thickness of 1.06 between the two airfoils. The unsteady pressure distributions of the two airfoils were also compared.[18] Although the steady shock strengths were different, the locations and widths of the unsteady shock pulses were very similar. It should also be noted that the unsteady pressures away from the shock were very similar for these two airfoils with very different aft steady pressure loading (cf. fig. 9). Thus, the resulting similarity of the flutter boundaries of the two airfoils (again with a shift of $\approx$ 0.01 in M) is to be expected.

Reference 18 also studied the effect of oscillation amplitude upon unsteady forces. The pressure distribution on the NACA 64A010A airfoil at M = 0.78 and k = 0.15 is shown in fig. 11 for pitching amplutide, α_0, of 0.25 to 2 deg. The pressures are normalized by oscillation amplutide and away from the shock there is very little effect of amplitude. The width of the shock pulse increases while its height decreases with increasing amplitude in such a way that overall forces are nearly linear with respect to amplitude. These features of similarity of unsteady forces with respect to varying airfoil shape, thickness, and motion amplitude point to the possibility of utilizing linear stability analysis methods at least on a local basis.[18] Note that this requires that forces vary reasonably linearly in motion amplitude and that forces due to different modes of motion may be superimposed reliably. The use of s-plane Pade' representations of the unsteady forces to perform such linear flutter calculations of airfoils at transonic speeds is demonstrated in Ref. 18. Flutter speeds predicted in this manner are within a few percent of those determined from direct transient responses.

Motion amplitudes for cases presented thus far have been small such that the small disturbance assumption was reasonable. Figure 12 presents results for larger amplitudes which press this assumption.[8] Comparisons of calculated and experimental lift and moment coefficients versus angle-of-attack are given for pitching amplitudes, α_0, up to 4.59 deg. and for mean pitch angles, α_m up to 4.86 deg. Agreement for the lift coefficients varies from very good to good. In contrast, the moment coefficients show a systematic difference between the calculated and experimental values. The characteristic shape of the c_m - α curves for the non-zero mean pitch angle cases, figs. 12(a-c), is caused by a large second harmonic contribution. In fig. 12(d), the different character of the c_m - α curve is due to the increased third harmonic component. These examples demonstrate the ability of the XTRAN2L code to predict with reasonable accuracy airloads due to moderately large airfoil motions for which the flow remains attached.

The next case to be presented illustrates the effect of varying reduced frequency. Comparison of computed and experimental unsteady airloads due to pitching for the 10.6-percent thick NACA 64A010A airfoil are given in figure 13. Also shown are Howlett's results[25] wherein an integral equation boundary layer model is coupled with the inviscid XTRAN2L code to compute viscous effects. At the test Mach number, M = 0.796, a moderate stength shock is located near midchord. The agreement of coefficients for the inviscid and viscous calculations is very good for $0.1 < k < 0.3$, whereas the computed moments are displaced from the experimental values. Below k = 0.1 the calculated lift coefficient and the real part of the moment coefficient deviate from experiment. The viscous corrections for this case are slight and do not correct for either the offset in the moment or the low frequency deviation. Fuglsang* shows that this low frequency deviation is corrected by his nonisentropic modifications.

Figures 9-13 demonstrate the effect of airfoil shape and oscillation amplitude on unsteady forces for moderate reduced frequencies. The effect of shape, thickness, camber, and angle-of-attack upon these forces for a wider range of frequencies are given by Batina.[26] The harmonic forces for airfoil plunge and pitch motions were computed using the pulse-transient technique and results are given for $0 < k < 1.0$. Shape effects were studied by considering three symmetric ten-percent thick airfoils: NACA 0010, NACA 64A010, and parabolic arc. Thickness effects were calculated for the 8, 10, and 12-percent thick NACA 0008, NACA 0010, and NACA 0012 airfoil sections. Angle-of-attack and camber effects were also considered. Figure 14 is typical of the results of this study, showing lift coefficient due to pitching for three airfoils at M = 0.78. At this Mach number, small supersonic regions have formed near the points of maximum thickness for all three airfoils: 0.3c for the NACA 0010, 0.4c for the NACA 64A010, and 0.5c for the parabolic-arc airfoil. Figure 13 is typical of the study in that: 1.) the three airfoils show similar trends with frequency, 2.) the moment coefficients are more sensitive to airfoil shape

*unpublished calculations.

than the lift coefficients and 3.) the difference between unsteady forces, where they exist, are such that the NACA 64A010 forces generally lie between those of the other airfoils for a given value of k (c.f. c_{m_α}). Note that the points of maximum thickness and location of formation of the supersonic region follow this same sequence. Of particular interest in the moment coefficient, c_{m_α}, is the clear evidence of an "aerodynamic resonance" near k = 0.6. Such resonances have been reported for measured unsteady airloads[27] where there is strong evidence of shock-induced flow separation. A key result of this study is that the differences in unsteady airloads for these airfoils are more closely related to maximum thickness locations, maximum steady pressure locations, and steady shock strengths rather than to differences in airfoil shape.

Unsteady Airloads were also studied for 8, 10, and 12 percent thick airfoils with similar shapes. At Mach numbers determined using steady transonic similarity scaling, the unsteady airloads for these airfoils have similar characteristics as functions of reduced frequency. The effects of differing thickness become less important with increasing thickness. Finally, effects of angle-of-attack and camber were investigated for the NACA 64A010 airfoil. When the steady shock position and strength are matched, the effects of angle-of-attack and camber upon the unsteady airloads were quite similar.

Three-Dimensional Airloads

Comparisons of steady and unsteady pressures calculated by the XTRAN3S code with experimental data have been reported in Refs. 19, 28, and 29. The first two experimental data sets are for rigid models oscillating in pitch while the latter is for an aeroelastic research wing which deformed significantly due to the test airloads.

The first case[19] involved a rectangular supercritical wing with a panel aspect ratio of 2. It was oscillated in pitch about 0.46 chord. The calculated and experimental steady pressures are compared in figure 15 for M = 0.7 and α = 2°. Calculations for both sets of coefficients, Eqs. 5 and 6, are shown. At this Mach number there is little difference in the results obtained using these coefficients except near the leading edge peak where use of the Eq. 6 coefficients results in a larger pressure gradient. At a higher Mach number[19], this effect is accentuated with the coefficients of Eq. 6 yielding a shock that is significantly stronger and located further aft than that predicted when using Eq. 5. The lack of agreement in the nose area shown in figure 15 is the result of using a relatively coarse grid near the nose.

Unsteady pressures for this case are shown in figure 16.[19] The reduced frequency is k = 0.356 and the Eq. 6 coefficients have been used. Also included for comparison are linear lifting surface theory results from the RHOIV code.[30] The magnitude of linear theory pressure is too low at the leading edge and too high at the trailing edge. The XTRAN3S results better predict the pressure peak at the nose and are in better agreement with experiment than linear theory over the rest of the wing. At this frequency, the phase angles are well predicted except near the tip. At lower frequencies[19], the phase angles show discrepancies over the aft 40 percent of chord, which is attributed to unmodeled viscous effects in the lower surface cove region.

The second model[28] was tested by the RAE and is referred to as the AGARD tailplane model. It has a 50 deg. leading edge sweep angle, a taper ratio of 0.27, and a NACA 64A010.2 airfoil section. Steady and unsteady pressures are given in figures 17 and 18. Steady pressure comparisons are good except near the tip. Comparisons of unsteady pressures at M = 0.65, 0.80 (not shown), and 0.86 (figure 18) show good agreement for trends, and good qualitative agreement for the inboard sections.

Bennett et al.[29] reported XTRAN3S calculatons for a flexible aeroelastic model of a transport-type wing. The supercritical wing model has an aspect ratio of 10.3 and a leading-edge sweepback angle of 28.8 deg. Wing thickness varies from 15 deg. at the root to 11 deg. at the tip, and the wing has a rather blunt leading-edge. For subcritical Mach numbers, only fair agreement of calculated steady pressures with experiment was obtained with the agreement being better in the outboard span region. At higher Mach numbers, the agreement deteriorated with calculations showing strong shocks where none were seen in the data.

An aeroelastic analysis of this model was performed using the first eight normal vibration modes. While no flutter boundaries were calculated, a very interesting correlation of static wing deformation was obtained which is given in figure 19. Although the calculated tip deflection, z_t, at 300 pounds/ft^2 (psf) dynamic pressure is approximately 40 percent high, the nonlinear feature of this loading versus dynamic pressure is predicted. The agreement seen in the tip twist angle, θ_t, is fortuitous in light of the poor steady pressure agreement for these conditions.

These examples indicate the level of accuracy of unsteady airloads calculated by the XTRAN3S code. The available grid size (60 x 40 x 20 points) is marginal and refined grids should improve accuracy. In addition, the recent developments in nonisentropic modeling, figures 6-8, and in viscous boundary layer modeling should be instrumental in improving correlation with experiment.

Aerodynamic Interference

The previous section presented details of the validation of the XTRAN3S code by comparison with experimental data from isolated wings. The code is also being augmented to enable calculations for complete aircraft. Batina has developed capability to model multiple lifting surfaces[11] and wing-fuselage[12] interference effects. Reference 11 gives examples of wing-tail and canard-wing interference effects.

Figure 20 gives canard and wing lift coefficients due to canard pitching at M = 0.9, α = 2°, and k = 0.3. The surfaces have similar planforms with 45° leading-edge sweep angle, 0.5 taper ratio, and NACA 0010 airfoil sections. Results for two separation distances are given: S = 0.25 and 0.5 (measured in terms of wing root chord). At this Mach number, the interference effect of the wing on the canard is small, with both XTRAN3S results, C_{ℓ_C}, lying near the isolated lifting surface line (also calculated by XTRAN3S). In contrast, the induced load on the wing, C_{ℓ_W}, is significant with an appreciable effect of separation distance seen in the real part. For the cases studied, interference effects were larger for the wing-tail configuration than for the canard-wing. Also, at M = 0.9 there was negligible induced interference effect on the forward surface for either configuration.

Capability for modeling wing-fuselage geometries is reported in Ref. 12. The fuselage is modeled by imposing body boundary conditions on a constant cross-section computational surface. The body boundary conditions are modified by slender body theory to account for the disparity with the actual surface. Comparisons with steady experimental wing-fuselage data are given for three configurations[12] and very good agreement is shown for fuselage pressures and for the interference effect on wing pressures. To assess the interference effect upon typical unsteady airloads, calculations were performed at M = 0.91 for an assumed wing first bending mode oscillating at k = 0.25. Figure 21 gives the resulting section lift and moment coefficients versus span for the wing-alone and for the wing-fuselage. Interference effects on the lift are largest inboard whereas the moment is affected both at the root and near midspan. The maximum effects on the integrated generalized airloads were five percent increase in magnitude and three degree increase in phase angle. Inclusion of these augmented capabilities in the XTRAN3S code is anticipated to significantly expand the ability to perform transonic aeroelastic analyses for complicated geometries.

Transonic Aeroelasticity

The previous sections have given examples of 2-D and 3-D unsteady airloads calculated by the XTRAN2L and XTRAN3S potential codes. Comparison with measured unsteady pressures has allowed an assessment of their accuracy. In this section, the use of these potential codes to study transonic aeroelasticity and flutter is described. A key factor will again be the locally linear nature of the transonic airloads calculated by these codes.

Berry et al.[31] studied viscous effects upon transonic flutter using the method of Ref. 26. Pitching and plunging degrees of freedom were assumed and transient response curve fits of airfoil response time histories yielded the frequency and damping for the aeroelastic modes. An s-plane root locus of a typical case is given in figure 22. The case studied is the MBB-A3 airfoil at M = 0.76 and α = 1.5°. The ordinate gives the normalized frequency and the abscissa the normalized damping of the plunge (bending) and pitch (torsion) modes. Root loci of both the inviscid and viscous models are given as functions of the square of the speed index, V. In addition, results from the stability analysis of the Pade' model derived for this case are superimposed. Note the significant shift in the bending locus when viscous effects are included; the dynamic pressure at flutter (σ = 0) increases by 40%.[31] Also of note is the reasonably close agreement of the (locally linear) Pade' model results with the time marching results; the viscous Pade' model over-predicts the flutter dynamic pressure by 11 percent.[31]

The importance of the coupling between static deformation and flutter for transonic aeroelasticity was shown by Edwards et al.[17] Flexible wings deform under load such that the wing tip tends to deflect towards negative twist angles as wing loading is increased. A 2-D analogy of this effect is to compute the twist caused by the static pitching moment upon the two degree-of-freedom pitch-plunge model. In this analogy, the reference position of the pitching spring is fixed to simulate a wing root angle-of-attack, α_r, and the airfoil pitching moment, c_m, twists this pitch spring, resulting in an airfoil angle-of-attack α. Figure 23 gives the resulting root locus[17] versus speed index, V, for the MBB-A3 supercritical airfoil at M = 0.775 and α_r = 3°. The root locus is annotated with speed index, V, and effective angle-of-attack, α. Also shown as inserts are the steady pressure distributions at V = 0.6, α = 1.0°, and V = 1.15, α = -0.5°. The effect of the increased loading as V increases is to twist the airfoil nose down, thus delaying the onset of transonic effects as seen in the pressure distributions. The net effect is to produce a local minimum in damping at M = 0.6. As V increases, the mode becomes damped again and finally flutters at V = 1.3. A small increase in either M or α_r would lead to flutter at V = 0.6. The flutter point at ω = 1.33 rad/sec corresponds to a classical type of flutter in which significant frequency coalescence occurs. The incipient flutter condition at ω = 85 rad/sec has much less frequency coalescence and is similar to cases which have been termed "single degree-of-freedom" or "shock-induced" flutter. Inspection of the pressure distributions corresponding to these two conditions indicates that the lower frequency flutter occurs when a very moderate shock has just developed on the upper surface. In Ref. 17, these features are attributed to the aft loading of the super-critical airfoil, and it is shown that this can lead to multiple flutter speeds for a given Mach number.

A final example of transonic aeroelasticity is provided by Batina and Yang.[32] They studied active control of transonic flutter for 2-D flow using the LTRAN2-NLR code. This code is very similar to the XTRAN2L code with the principal exception being the omission of the Φ_{TT} term in Eq. 1. They also determined the suitability of the locally linear Pade' model for studying airfoil stability. Active feedback stabilization of a flutter mode was demonstrated using three simplified feedback laws: plunging position, velocity, and acceleration.

Figure 24 summarizes the acceleration feedback study with the control surface position, δ, given by $\delta = K_A \ddot{h}$ where K_A is the feedback gain. A composite of two root-locii is shown: open-loop locus leading to flutter at $V/V_f = 1.0$ and the closed-loop locus resulting from increasing the acceleration feedback gain, K_A, at $V/V_f = 1.0$. As shown, the bending mode is stabilized and the torsion mode destabilized by the feedback control. Significantly, the Pade' model works very well for this case involving aft-airfoil control surface motions. This further demonstrates the locally linear nature of transonic airloads computed by TSD computer codes.

Concluding Remarks

Calculations from two transonic small disturbance (TSD) equation computer codes have been presented and compared with experimental results in order to demonstrate the ability of potential equation codes to treat transonic effects. The two-dimensional XTRAN2L code and the three-dimensional XTRAN3S code were used to demonstrate the effects of several parameter variations upon unsteady airloads. The importance of the computational grid and far-field boundary conditions was illustrated by examples of reflections from boundaries and from large grid stretching in the near-field. The use of nonreflecting boundary conditions enables use of an economical computational grid covering an extent of ±25 chordlengths in the z-direction.

Conservative potential equation solutions do not account for entropy generated within shocks and can be in serious disagreement with more exact Euler equation solutions. In extreme cases, multiple solutions are found in both 2-D and 3-D flows and, at lower transonic Mach numbers, lift-curve slopes can be seriously in error. Low frequency unsteady airloads are particularly prone to error due to this effect. Nonisentropic corrections to the transonic small disturbance equation alleviate these shortcomings and provide results similar to Euler equation results.

Examples from the XTRAN2L code illustrate a variety of significant effects. A key observation is the degree to which calculated unsteady airloads from transonic inviscid potential equation codes are locally linear with respect to motion amplitude and mode of motion. Thus, linear superposition methods may be applied to study aeroelastic stability and Pade' representation transonic aeroelastic models give acceptable accuracy and are very economical. Investigations of airfoil shape and thickness effects indicate that differences in unsteady airloads are more closely related to the locations of maximum airfoil thickness and maximum steady pressure location on the airfoil rather than to differences in the airfoil shape.

Three examples from the XTRAN3S code provide comparisons with experimental data from: a rectangular supercritical wing model oscillating in pitch, a swept tailplane model oscillating in pitch, and a flexible aeroelastic model exhibiting considerable static deformation. Agreement of the calculated pressures with experiment is fair to good. The comparisons show instances where viscous modeling is required and also indicate a need for denser computational grids than have been available. The 3-D code is being extended to allow treatment of complete aircraft and examples of calculated canard-wing and wing-fuselage interference are given.

Finally, several examples of transonic aeroelastic calculations using the XTRAN2L code are given. For one case considered, inclusion of a viscous boundary layer model increased the predicted dynamic pressure at flutter by 40 percent. The key importance of the coupling between static and unsteady airloads for transonic aeroelastic effects is stressed. Multiple flutter speeds can occur at a given Mach number when static deformation is taken into consideration.

References

[1]Bland, S. R.: "AGARD Two-Dimensional Aeroelastic Configurations." AGARD AR156, August 1979.

[2]Bland, S. R.: "AGRAD Three-Dimensional Aeroelastic Configurations." AGARD AR167, March 1982.

[3]Anon.: "Compendium of Unsteady Aerodynamic Measurements. "AGARD R-702, August 1982.

[4]Anon.: "Transonic Unsteady Aerodynamics and Its Aeroelastic Applications." AGARD-CP-374, January 1985.

[5]Ballhaus, W. F.; and Goorjian, P. M.: "Implicit Finite-Difference Computations of Unsteady Flows about Airfoils." AIAA Journal, Vol. 15, December 1977, pp. 1728-1735.

[6]Whitlow, Woodrow, Jr.: "A Program for Solving the General-Frequency Unsteady Transonic Small Disturbance Equation." NASA TM 85723, November 1983.

[7]Borland, C. J.; and Rizzetta, D. P.: "Nonlinear Transonic Flutter Analysis." AIAA Journal, Vol. 20, No. 11, November 1982, pp. 1606-1615.

[8]Edwards, J. W.; Bland, S. R.; and Seidel, D. A.: "Experience with Transonic Unsteady Aerodynamic Calculations," In Transonic Unsteady Aerodynamics and Its Aeroelastic Applications, AGARD-CP-374, January 1985.

[9]Goorjian, P. M.; and Guruswamy, G. P.: "Unsteady Transonic Aerodynamic and Aeroelastic Calculations About Airfoils and Wings," In Transonic Unsteady Aerodynamics and Its Aeroelastic Applications, AGARD-CP-374, January 1985.

[10]Batina, J. T.: "Unsteady Transonic Flow Calculations for Two-Dimensional Canard-Wing Configurations with Aeroelastic Applications," AIAA Paper No. 85-0585, presented at the AIAA/ASME/ASCE/AHS 26th Structures, Structural Dynamics and Materials Conference, Orlando, Florida, April 15-17, 1985.

[11]Batina, J. T.: "Unsteady Transonic Flow Calculations for Interfering Lifting Surface Configurations," AIAA Paper No. 85-1711, presented at the AIAA 18th Fluid Dynamics, Plasma Dynamics and Lasers Conference, Cincinnati, Ohio, July 16-1, 1985.

[12]Batina, J. T.: "Unsteady Transonic Flow Calculations for Wing-Fuselage Configurations." AIAA paper No. 86-0862, presented at the AIAA/ASME/ASCE/AHS 27th Structures, Structural Dynamics and Materials Conference, San Antonio, Texas, May 19-21, 1986.

[13]Ruo, S. Y.; Malone, J. B.; and Sankar, L. N.: "Steady and Unsteady Full Potential Calculations for High and Low Aspect Ratio Supercritical Wings," AIAA Paper No. 86-0122, presented at the AIAA 24th Aerospace Sciences Meeting, Reno, Nevada, January 6-9, 1986.

[14]Shankar, V.; Ide, H.; Gorski, J.; and Osher, S.: "A Fast, Time-Accurate Unsteady Full Potential Scheme," AIAA Paper 85-1512, presented at the AIAA Computational Fluid Dynamics Conference, Cincinnati, 1985.

[15]Whitlow, W., Jr.; and Seidel, D. A.: "Nonreflecting Boundary Conditions for the Complete Unsteady Transonic Small-Disturbance Equation." AIAA Journal, Vol. 23, No. 2, February 1985, pp. 315-317.

[16]Seidel, D. A.; Bennett, R. M.; and Whitlow, W., Jr.: "An Exploratory Study of Finite Difference Grids for Transonic Unsteady Aerodynamics." NASA TM 84583, December 1982.

[17]Edwards, J. W.; Bennett, R. M.; Whitlow, W., Jr.; and Seidel, D. A.: "Time-Marching Transonic Flutter Solutions Including Angle-of-Attack Effects." Journal of Aircraft, Vol. 20, No. 11, November 1983, pp. 899-906.

[18]Bland, S. R.; and Edwards, J. W.: "Airfoil Shape and Thickness Effects on Transonic Airloads and Flutter." Journal of Aircraft, Vol. 21, No. 3, March 1984, pp. 209-217.

[19]Seidel, D. A.; Bennett, R. M.; and Ricketts, R. H.: "Some Recent Applications of XTRAN3S." AIAA paper No. 83-1811, presented at the AIAA Applied Aerodynamics Conference, Danvers, MA, July 13-15, 1983.

[20]Salas, M. D.; and Gumbert, C. R.: "Breakdown of the Conservative Potential Equation," AIAA Paper No. 85-0367, presented at the AIAA 23rd Aerospace Sciences Meeting, Reno, Nevada, January 14-17, 1985.

[21]Steinhoff, J.; and Jameson, A.: "Multiple Solutions of the Transonic Potential Flow Equation. AIAA Journal, Vol. 20, No. 11, 1982, pp. 1521-1525.

[22]Williams, M. H.; Bland, S. R.; and Edwards, J. W.: "Flow Instabilities in Transonic Small-Disturbance Theory." AIAA Journal, Vol. 23, No. 10, October 1985, pp. 1491-1496.

[23]Fuglsang, D. F.; and Williams, M. H.: "Non-Isentropic Unsteady Transonic Small Disturbance Theory," AIAA Paper No. 85-0600, presented at the AIAA/ASME/ASCE/AHS 26th Structures, Structural Dynamics and Materials Conference, Orlando, Florida, Aril 15-17, 1985.

[24]Gibbons, M. D.; Whitlow, W., Jr.; and Williams, M. H.: "Nonisentropic Unsteady Three Dimensional Small Disturbance Potential Theory," AIAA Paper No. 86-0863, presented at the AIAA/ASME/ASCE/ASH 27th Structures, Structural Dynamics and Materials Conference, San Antonio, Texas, May 19-21, 1986.

[25]Howlett, J. T.: "Efficient Self-Consistent Viscous-Inviscid Solutions for Unsteady Transonic Flow," AIAA Paper No. 85-0482, presented at the AIAA 23rd Aerospace Sciences Meeting, Reno, Nevada, January 14-17, 1985.

[26]Batina, J. T.: "Effects of Airfoil Shape, Thickness, Camber, and Angle of Attack on Calculated Transonic Unsteady Airloads." NASA TM 86320, March 1985.

[27]Hounjet, M. L. H.; and Meijer, J. J.: "Application of Time-Linearized Methods to Oscillating Wings in Transonic Flow and Flutter," in Transonic Unsteady Aerodynaics and Its Aeroelastic Applications. AGARD-CP-374, January 1985.

[28]Bennett, R. M.; Wynne, E. C.; and Mabey, D. G.: "Cal-,culations of Transonic Steady and Oscillatory Pressures on a Low Aspect Ratio Model and Comparison with Experiment," Paper No. 85-17, presented at the Second International Symposium on Aeroelasticity and Structural Dynamics,Technical University of Aachen, Germany, April 1-3, 1985.

[29]Bennett, R. M.; Seidel, D. A.; and Sandford, M. C.: "Transonic Calculations for a Flexible Supercritical Wing and Comparison with Experiment," AIAA Paper No. 85-0665, presented at the AIAA/ASME/ASCE/AHS 26th Structures, Structural Dynamics and Materials Conference, Orlando, Florida, April 15-17, 1985.

[30]Redman, M. C.; and Rowe, W. S.: "Prediction of Unsteady Aerodynamic Loadings Caused by Leading Edge Control Surface Motions in Subsonic Compressible Flow--Computer Program Description." NASA CR 132634, May 1974.

[31]Berry, H. M.; Batina, J. T.; and Yang, T. Y.: "Viscous Effects on Transonic Airfoil Stability and Response." AIAA Paper No. 85-0586, presented at the AIAA/ASME/ASCE/ASH 26th Structures, Structural Dynamics and Materials Conference, Orlando, FL, April 15-17, 1985.

[32]Batina, J. T.; and Yang, T. Y.: "Transonic Time Responses of the MBB A-3 Supercritical Airfoil Including Active Controls." Journal of Aircraft, Vol. 22, No. 5, May 1985, pp. 393-400.

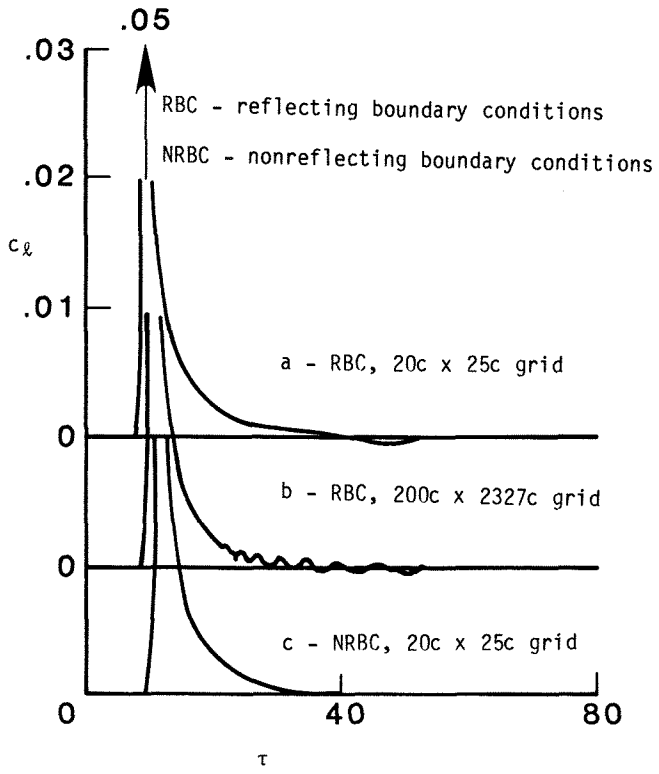

Figure 1. Lift coefficient time histories due to pulsed pitching motion for flate plate airfoil at M = 0.85.

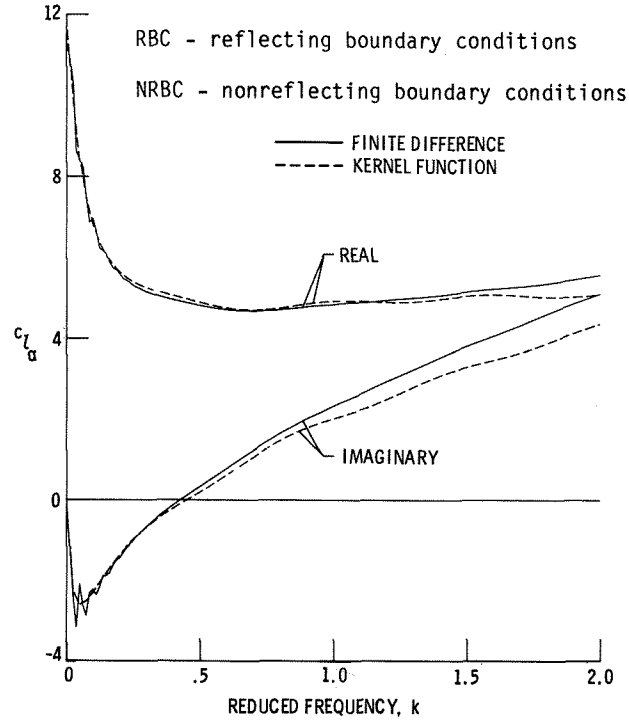

a) RBC, 20c x 25c grid

Figure 2. Lift coefficient frequency response functions due to pulsed pitching motion for flap plate airfoil at M = 0.85.[16]

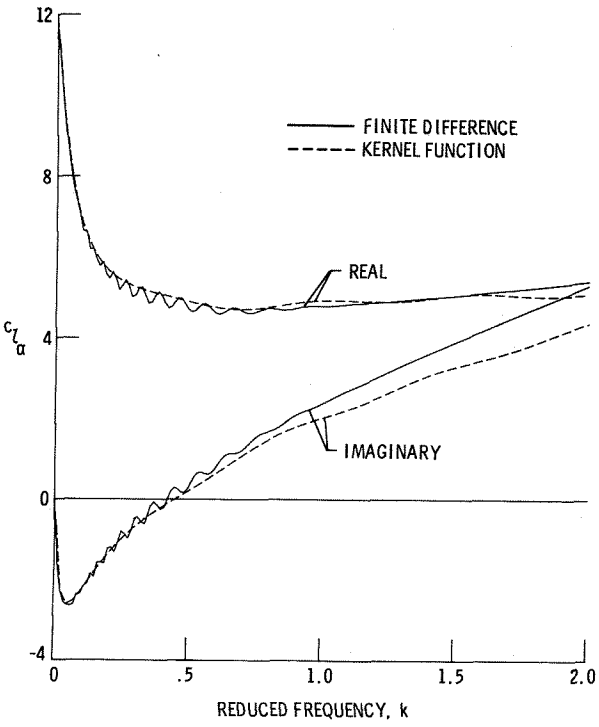

b) RBC, 200c x 2327c grid

Figure 2. continued

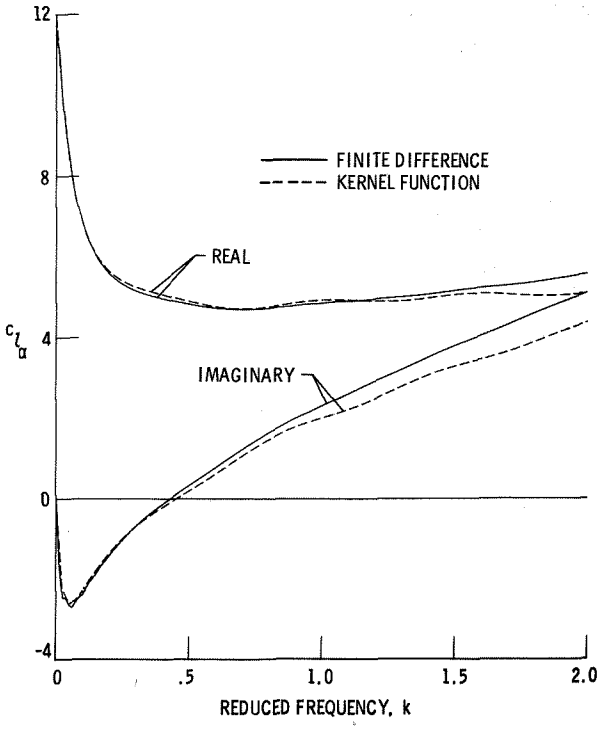

c) NRBC, 20c x 25c grid

Figure 2. Concluded

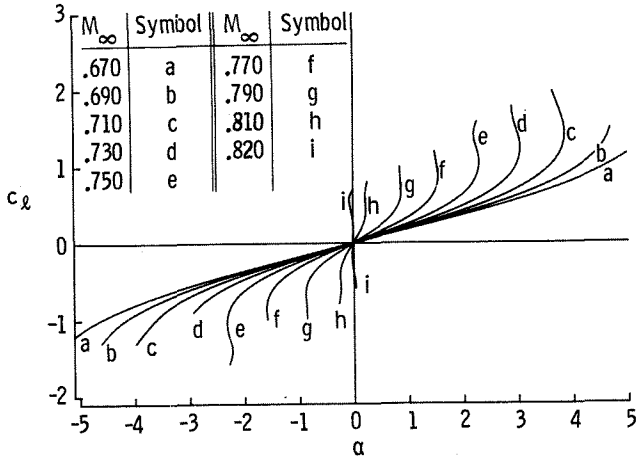

Figure 3. Lift-curve for NACA 0012 airfoil computed with FL036 code versus angle-of-attack as a function of Mach number.[20]

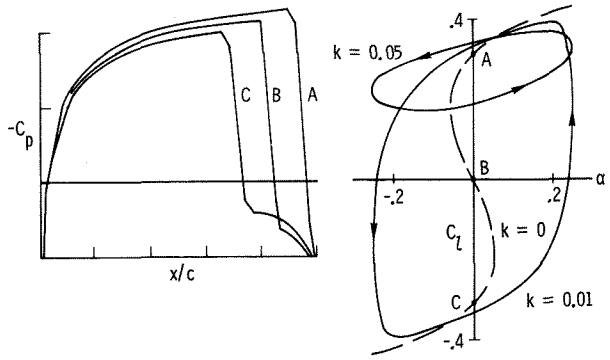

Figure 4. Anomalous behavior of potential flow solutions for NACA 0012 airfoil at M = 0.85, α_m = 0.[8]

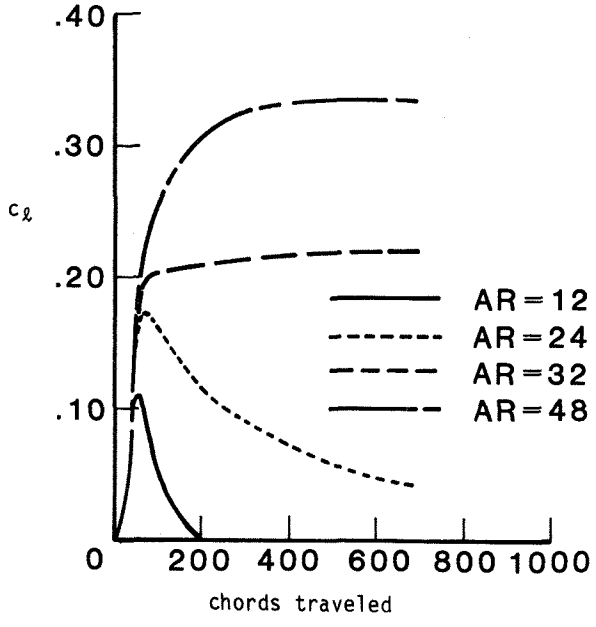

Figure 6. Lift coefficient time histories due to pitch pulse for the NACA 0012 wing at M = 0.84 as a function of aspect ratio.[24]

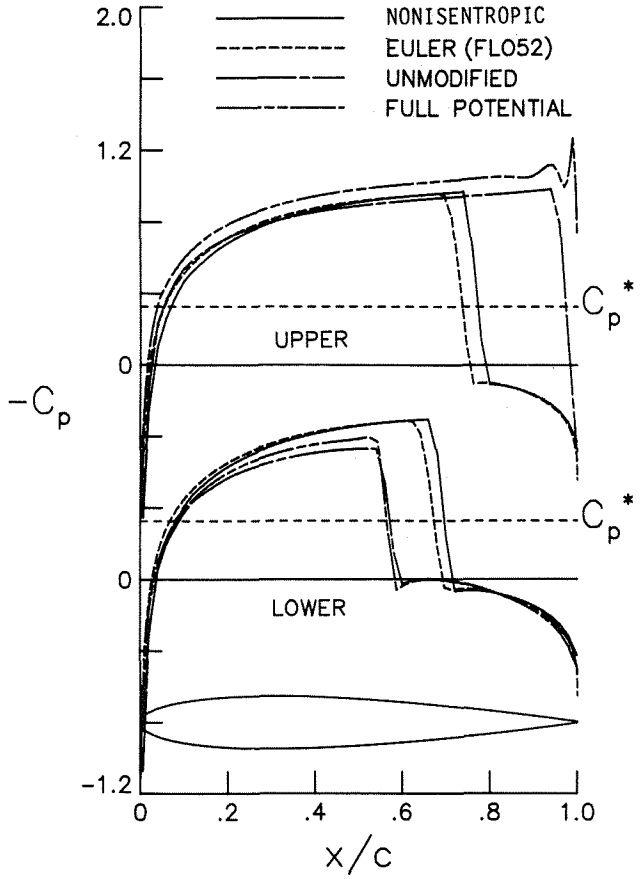

Figure 5. Steady pressure distribution for NACA 0012 airfoil at M = 0.84, α_m = 0.25°.[23]

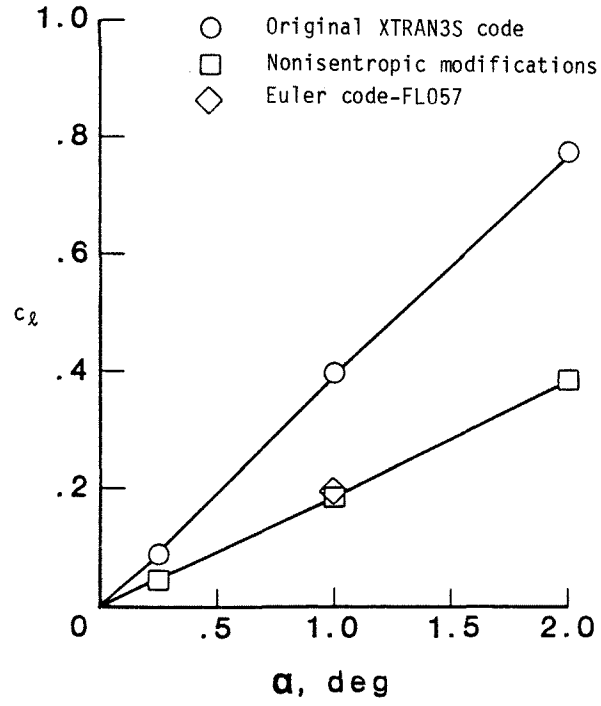

Figure 7. Total lift coefficient for NACA 0012 wing with AR = 12 at M = 0.82.[24]

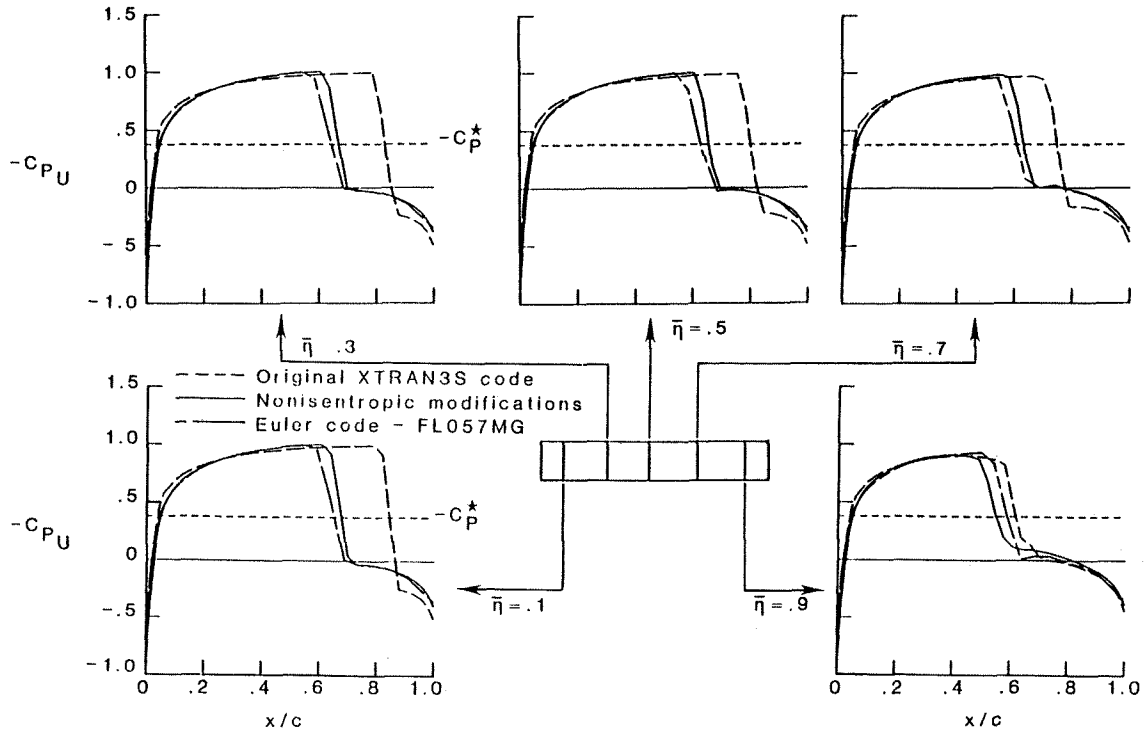

Figure 8. Steady pressure distribution on NACA 0012 wing with AR = 12 at M = 0.82, $\alpha = 1°$.[24]

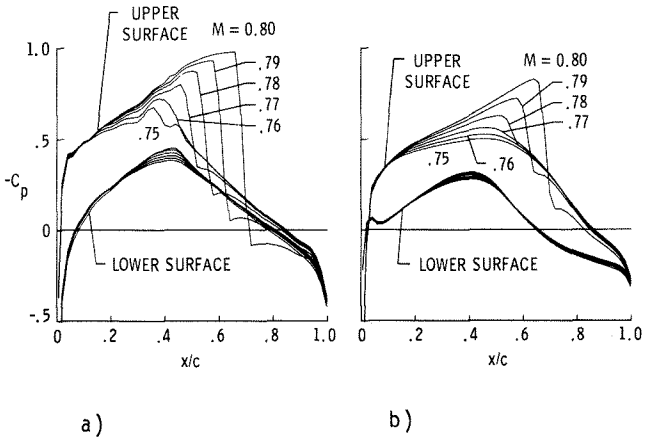

Figure 9. Steady pressure distributions;
a) NACA 64A010A airfoil, $\alpha = 1°$,
b) MBB-A3 airfoil, $\alpha = 0.5°$.[18]

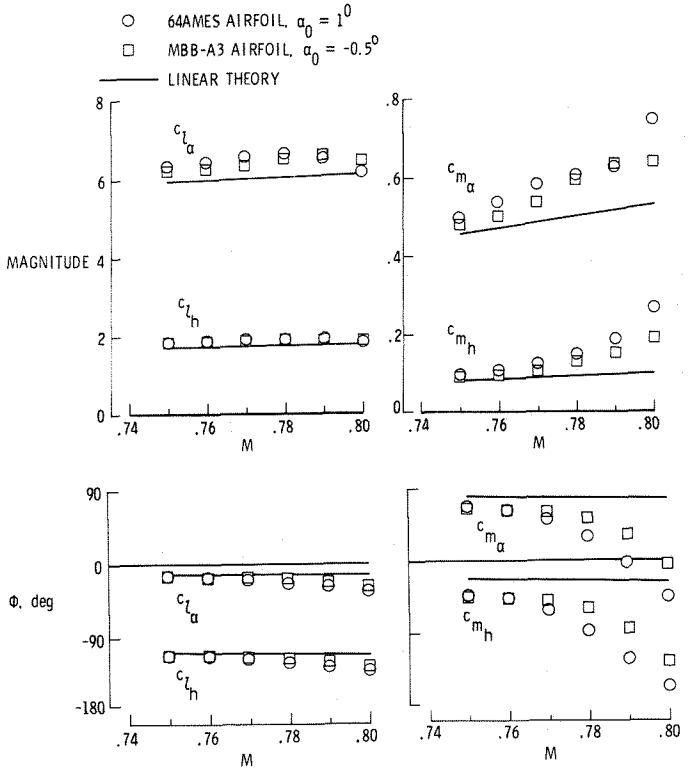

Figure 10. Unsteady airloads for NACA 64A010A and MBB-A3 airfoils versus Mach number, k = 0.15.[18]

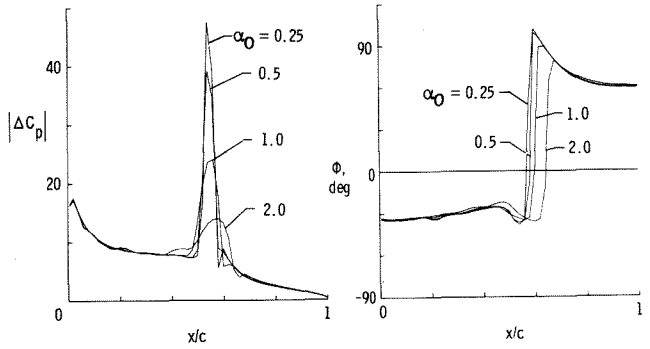

Figure 11. Pitch amplitude effect upon normalized pressure distribution for NACA 64A010A airfoil at M = 0.78, k = 0.15.[18]

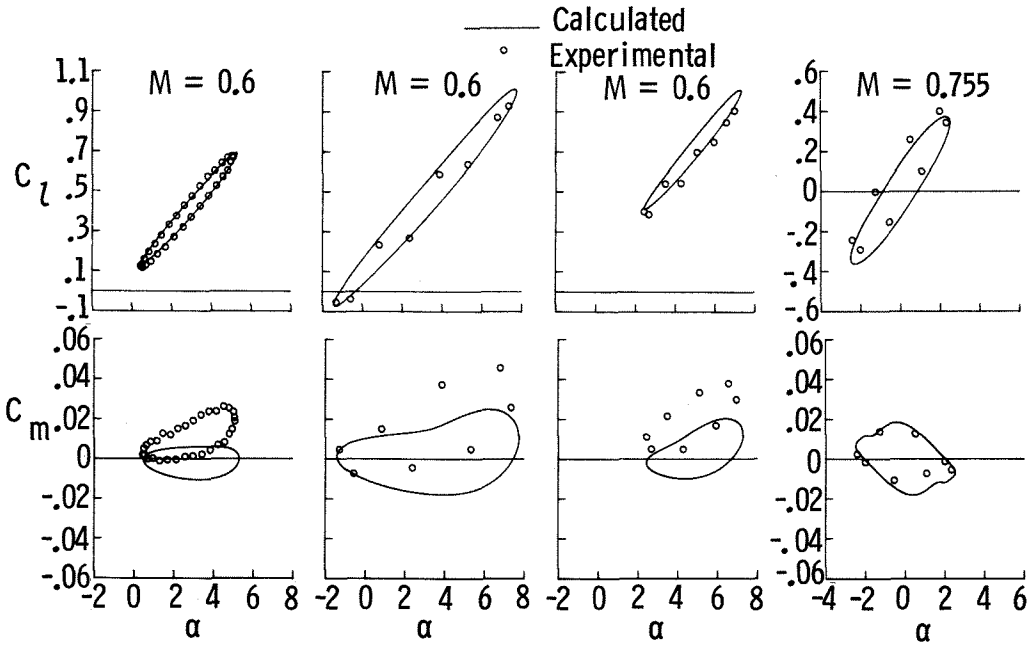

a) M = 0.6
α_m = 2.89°
α_0 = 2.41°

b) M = 0.6
α_m = 3.16°
α_0 = 4.59°

c) M = 0.6
α_m = 4.86°
α_0 = 2.44°

d) M = 0.755,
α_m = 0°
α_0 = 2.51°

Figure 12. Comparison of unsteady forces for the NACA 0012 airfoil at k = 0.081.[8]

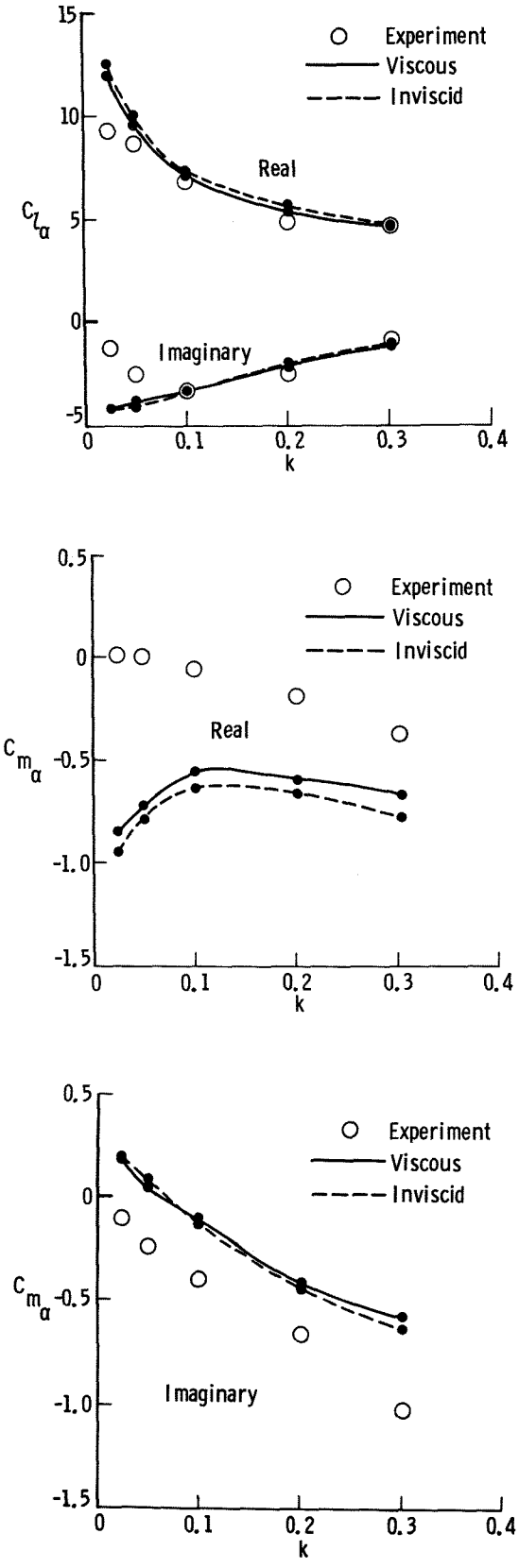

Figure 13. Comparison of unsteady forces for the NACA 64A010A airfoil at M = 0.796, α_0 = 1°.[25]

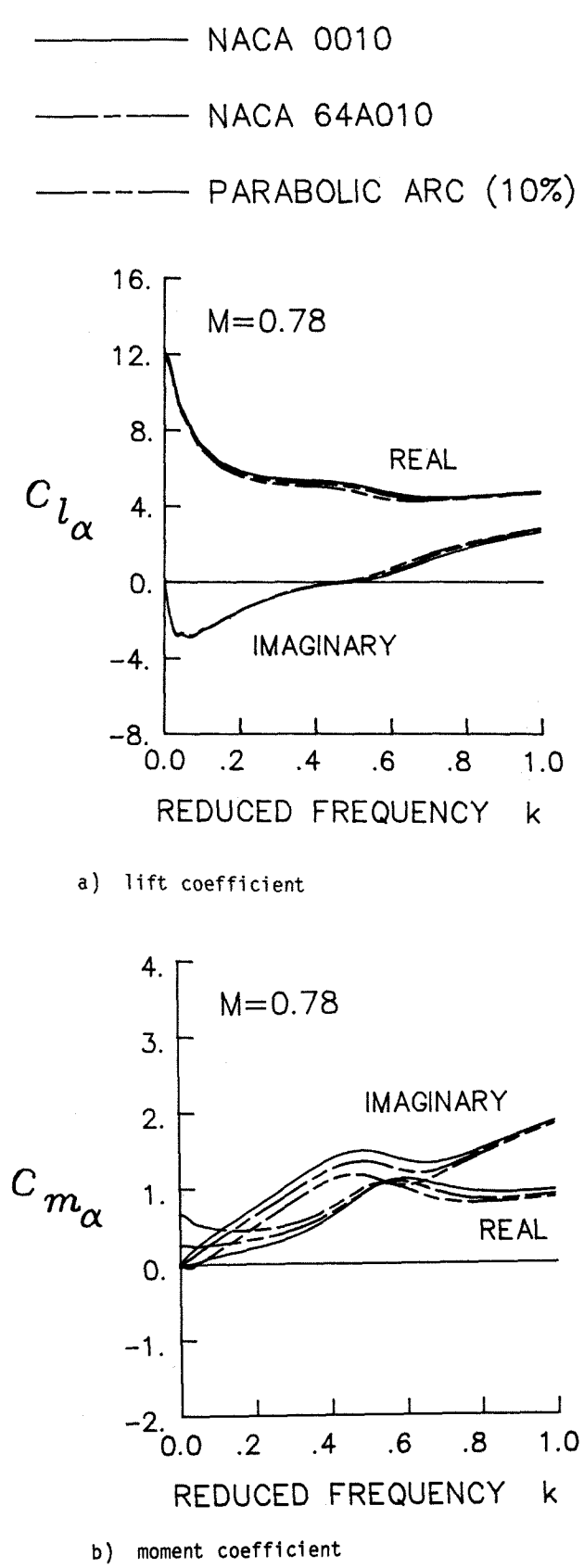

Figure 14. Comparison of airfoil shape effects upon unsteady forces for pitching oscillation at M = 0.78.[26]

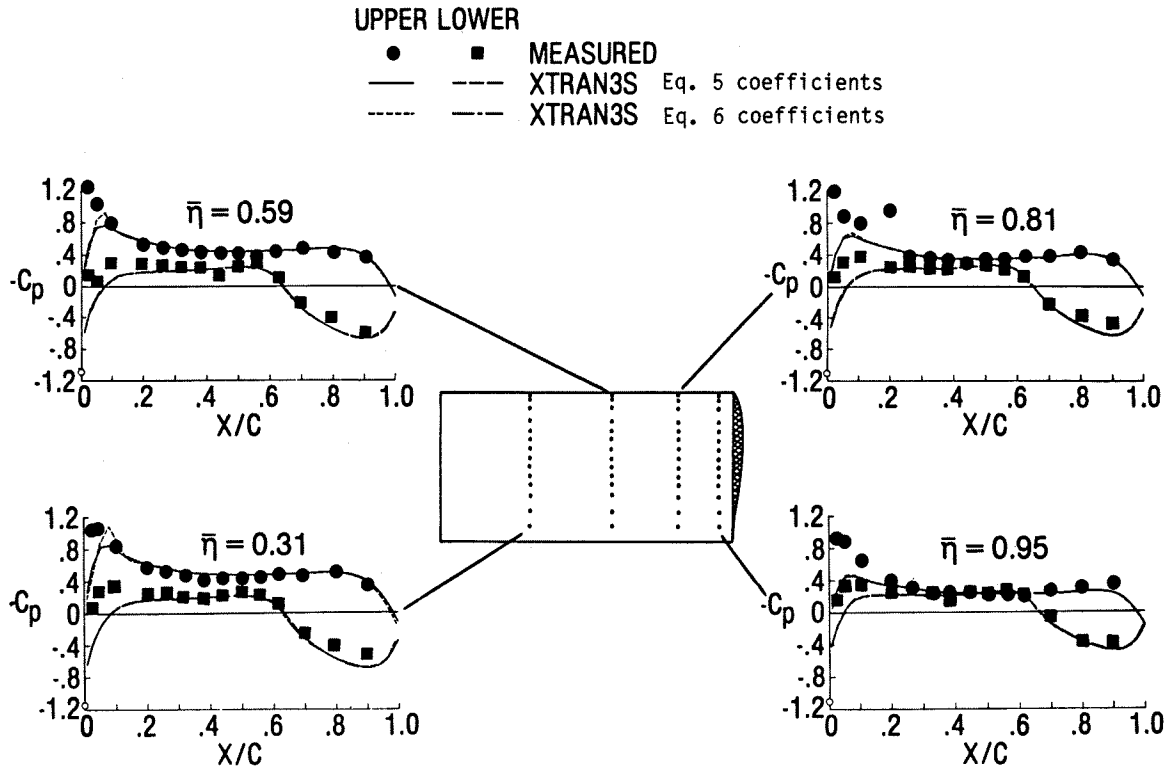

Figure 15. Comparison of measured and calculated steady pressure distributions for rectangular supercritical wing at M = 0.7, α_m = 2°.[19]

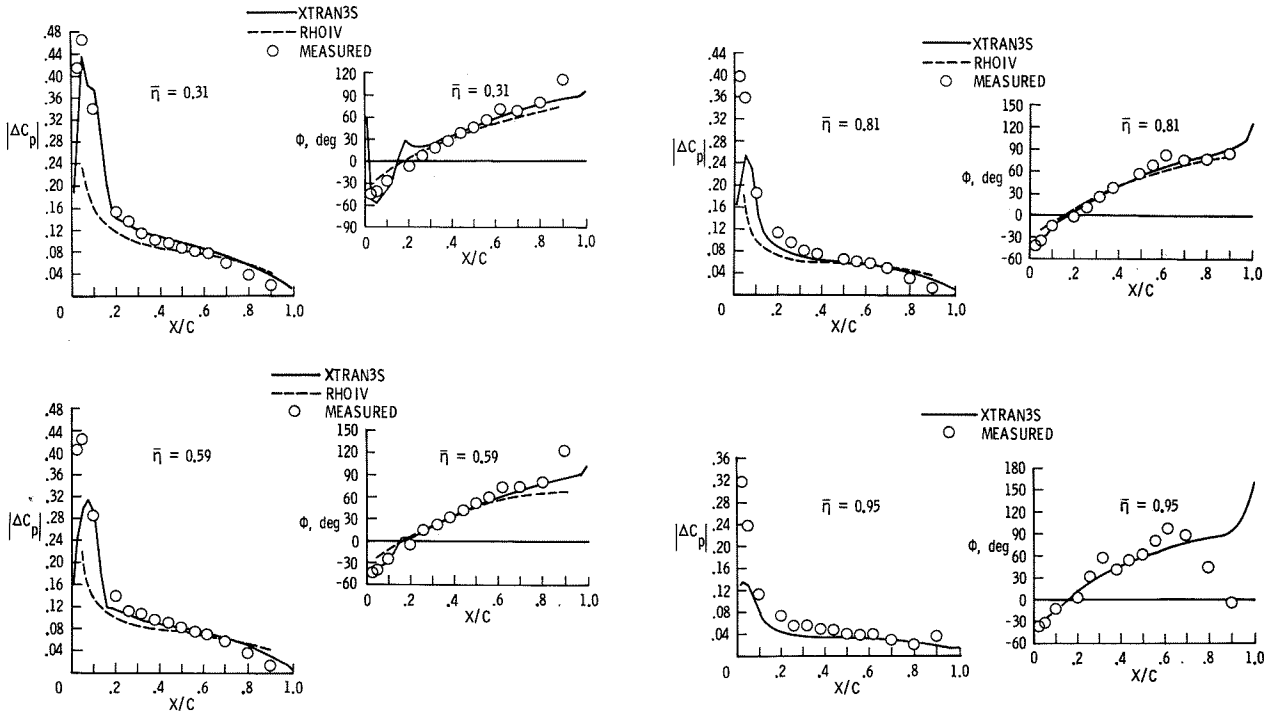

Figure 16. Comparison of measured and calculated unsteady pressure distributions for rectangular supercritical wing at M = 0.7, α_0 = 1°, k = 0.356.[19]

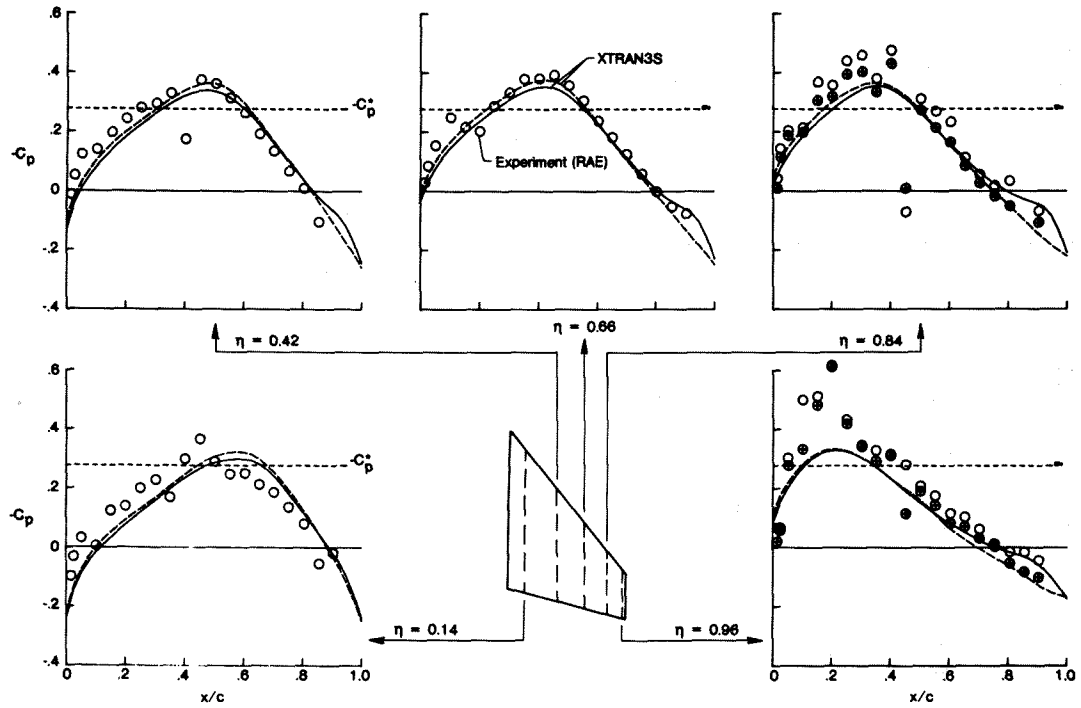

Figure 17. Comparison of measured and calculated steady pressure distributions for RAE tailplane model for M = 0.86.[28]

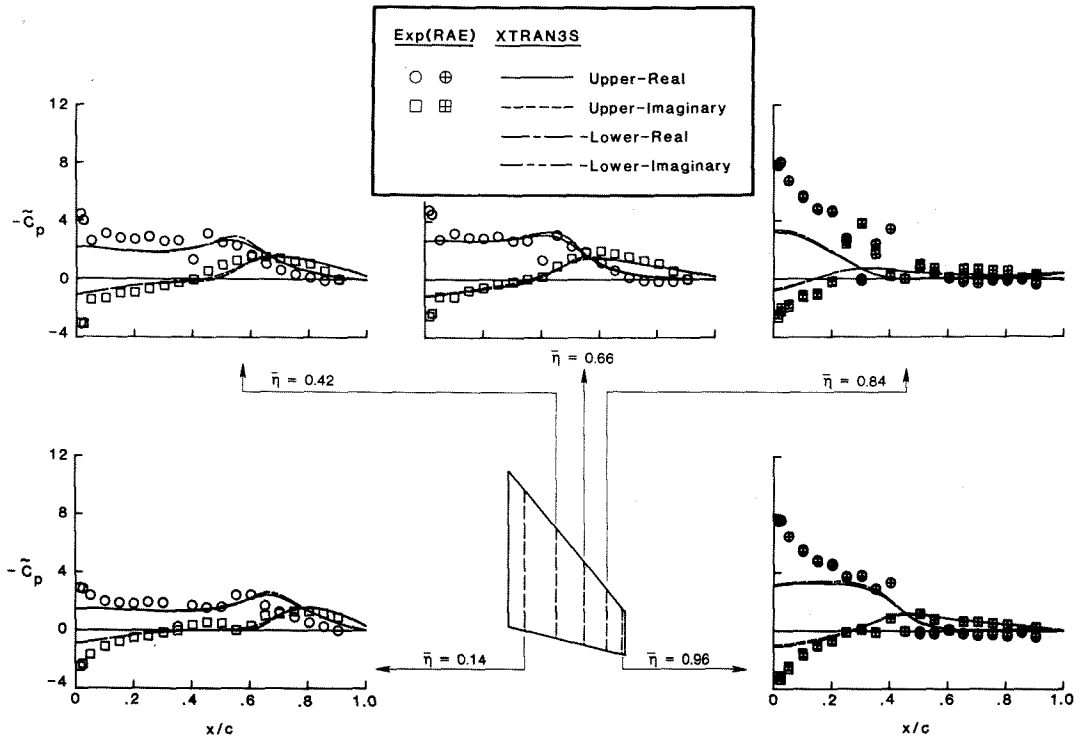

Figure 18. Comparison of measured and calculated unsteady pressure distributions for RAE tailplane model for M = 0.86, k = 4.56.[28]

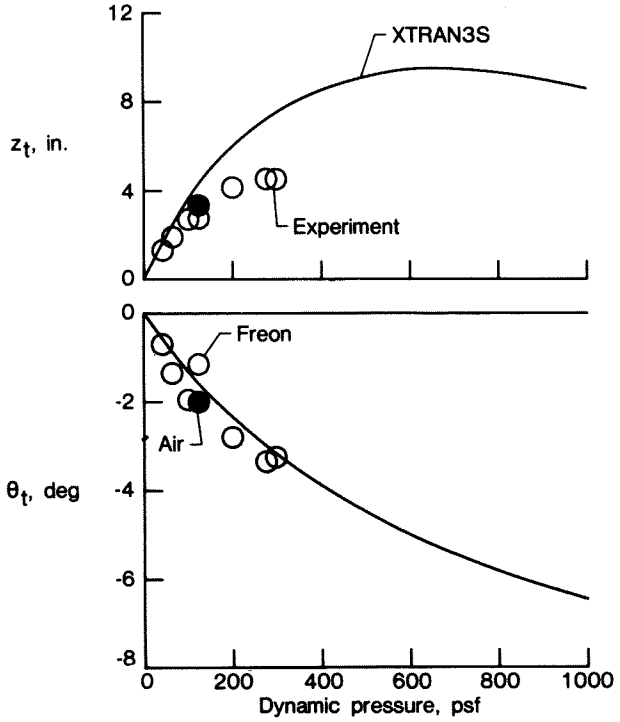

Figure 19. Comparison of measured and calculated wing-tip displacement and twist versus dynamic pressure for a flexible aeroelastic model, M = 0.8, $\alpha = 0°$.[29]

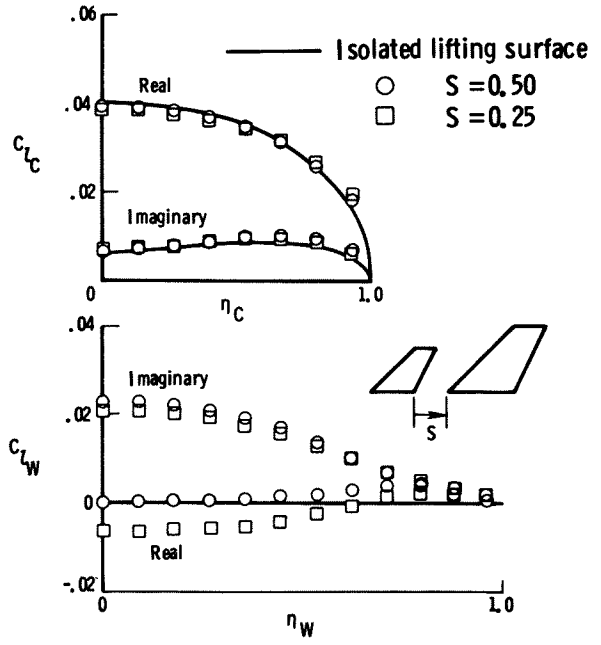

Figure 20. Unsteady sectional lift coefficients on canard-wing configuration due to canard pitching at M = 0.9, α_m = 2°, and k = 0.3.[11]

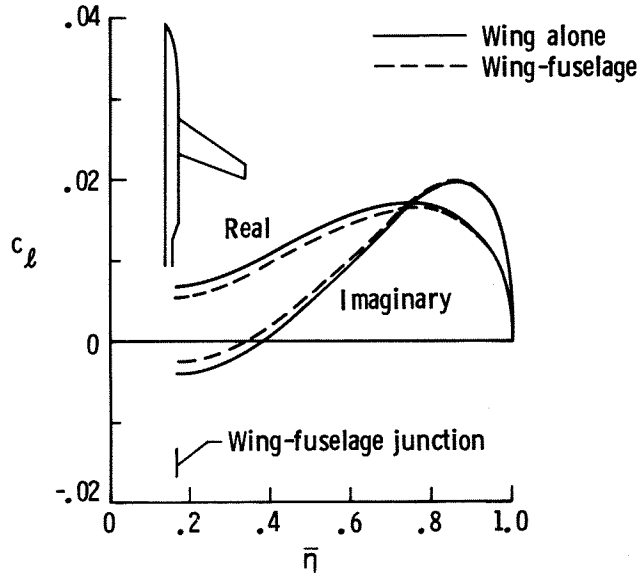

a) sectional lift coefficient

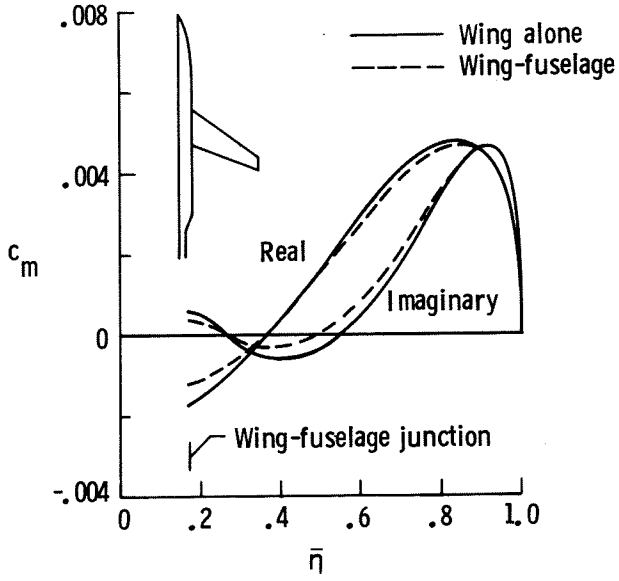

b) sectional moment coefficient

Figure 21. Unsteady sectional coefficients due to asumed wing first bending mode for the RAE wing-fuselage at M = 0.91, α = 1°, k = 0.25.[12]

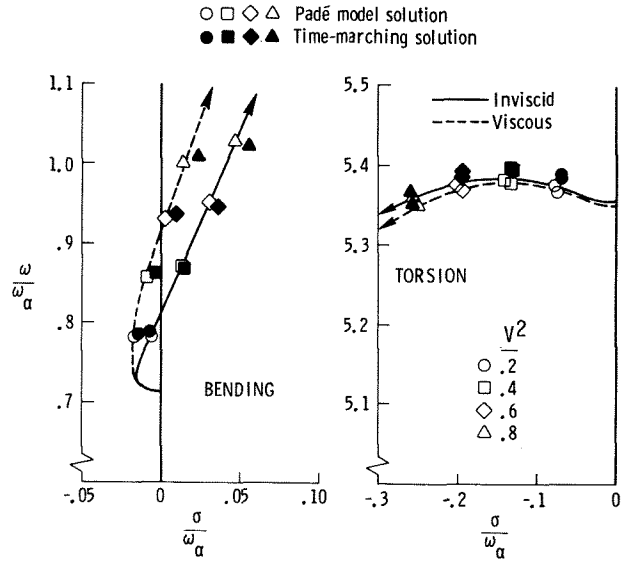

Figure 22. Effects of viscosity on airfoil stability as determined by time integration and by Pade' model; MBB-A3 airfoil, M = 0.765, α_m = 1.5°.[31]

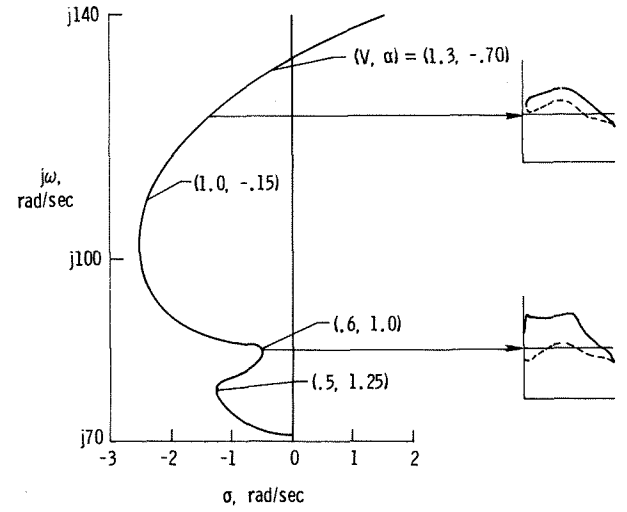

Figure 23. Flutter mode root-locus versus V for MBB-A3 airfoil suspended on pitch spring for M = 0.775, α_r = 3°.[17]

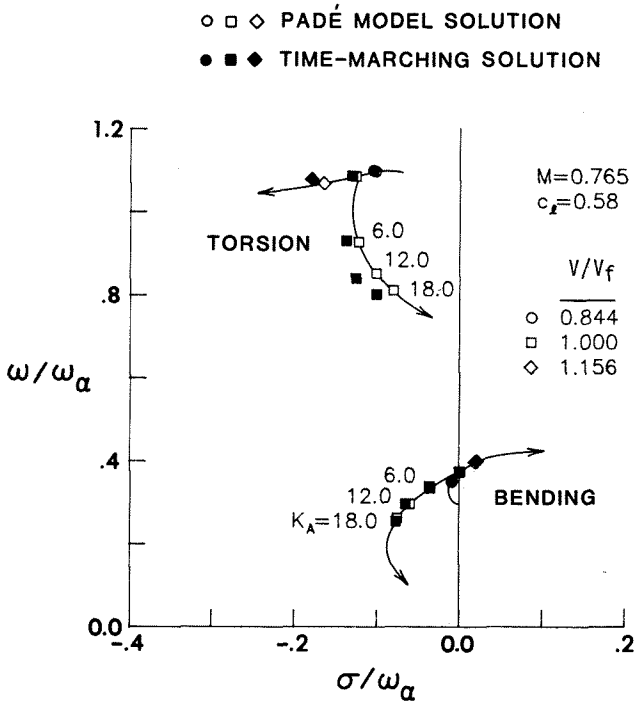

Figure 24. Effect of plunge acceleration feedback on MBB-A3 bending and torsion modes at the open-loop flutter speed.[32]